

A Modular Ray Tracing Framework for Optimizing VUV Flashlamp-to-Fiber Coupling Systems

Turja Roy, Dr. Jonathan Abraham Asaadi, Dr. Varghese Anto Chirayath

Department of Physics, University of Texas at Arlington, Arlington, TX 76019, USA

Abstract

A comprehensive ray tracing methodology is presented for optimizing two-lens coupling systems for vacuum ultraviolet (VUV) flashlamp-to-fiber applications with realistic experimental constraints. The system couples 200 nm light from a Hamamatsu L7685 60W xenon flashlamp (3 mm arc) with E6611 cooling jacket into a 1 mm fiber core ($NA = 0.22$). The cooling jacket imposes critical geometric constraints: lens positioning constrained to $z \geq 27$ mm and angular acceptance limited to 22.85° , introducing 43% geometric vignetting loss. Six optimization algorithms—grid search, Powell's method, differential evolution, Nelder-Mead simplex, dual annealing, and Bayesian optimization—are systematically compared using deterministic ray tracing with atmospheric absorption modeling. Systematic analysis identifies optimal configurations achieving coupling efficiencies up to 0.30 in argon atmosphere at 200 nm, representing realistic performance under cooling jacket constraints. Powell's method emerges as the recommended algorithm for routine optimization, providing rapid convergence (0.5 s per lens pair) and reliable performance. Combined atmospheric oxygen absorption and extended path lengths (optical system $L \approx 67$ mm) create substantial medium-dependent effects: systematic comparison reveals 32–33% relative coupling improvement in argon versus air at 200 nm for cooling-jacket-constrained configurations. Wavelength dependence analysis (150–300 nm) establishes chromatic performance characteristics and validates wavelength-dependent material modeling. Tolerance analysis establishes practical alignment requirements for laboratory implementation. The framework provides both a practical design tool incorporating realistic experimental constraints and methodological insights for non-convex optical optimization problems.

1 Introduction

Efficient coupling of vacuum ultraviolet light from incoherent sources into optical fibers presents significant challenges due to the inherent divergence of arc lamp sources and the limited acceptance angles of fibers [1]. The Hamamatsu L7685 60W xenon flash lamp provides a compact broadband source (190–2000 nm) suitable for liquid argon purity monitoring applications in the VUV/DUV range. This work focuses on optimizing coupling at the design wavelength of 200 nm, where fiber-optic delivery enables remote sensing and flexible optical system configurations in cryogenic environments.

The design of compact coupling optics requires balancing multiple objectives: maximizing coupling efficiency, minimizing physical length, and maintaining practical manufacturability with commercially available optical components. Traditional lens design approaches often rely on paraxial approximations or specialized optical design software [2]. However, the large numerical aperture and wide divergence angles in Xe

flashlamp systems necessitate full ray tracing to accurately predict system performance.

In this work, a stratified ray tracing framework is developed that incorporates realistic source geometry, lens specifications, fiber acceptance criteria, and atmospheric absorption effects (O_2 , N_2 , and H_2O). The design problem is formulated as a multi-objective optimization task, and six distinct optimization algorithms are systematically compared to identify lens positioning that maximizes performance. This approach provides both a practical design tool and insights into the efficacy of various optimization strategies for optical systems with complex, non-convex objective functions characterized by multiple local optima and discrete ray-counting mechanics that preclude analytical gradient computation.

2 System Description

2.1 Optical Configuration

The optical system comprises a Hamamatsu L7685 60W xenon flash lamp [3] with Hamamatsu E6611 cooling jacket, two fused silica lenses, and a multi-mode optical fiber [4] arranged along a common

optical axis. The lamp emits broadband radiation (190–2000 nm) from a compact 3.0 mm diameter arc; this work analyzes coupling performance at $\lambda = 150$ –300 nm.

The lamp assembly includes a protective Single Crystal Sapphire Glass window (14.3 mm diameter) positioned 8.7 mm from the arc. Critically, the Hamamatsu E6611 cooling jacket surrounds the lamp housing and constrains the optical aperture through its M23 threaded exit port (inner diameter 23 mm) located approximately 26 mm from the arc center. This cooling jacket imposes both geometric constraints on lens positioning and vignetting losses on the emitted light, as detailed in Section 2.2. The two-lens relay system is positioned after the cooling jacket exit to collect and refocus the divergent light into the fiber.

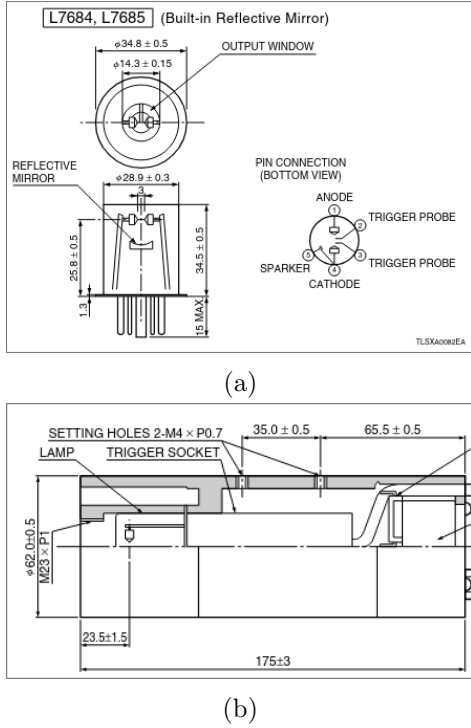


Figure 1: Dimensional Outline of (a) Hamamatsu L7685 Xenon Flash Lamp and (b) Hamamatsu E6611 Cooling Jacket (Unit: mm)

2.2 Source Characteristics

The xenon arc source exhibits a spatially extended emission profile with angular divergence constrained by the cooling jacket geometry. The source is modeled as emitting rays from a circular disk of radius $r_{\text{arc}} = 1.5$ mm with angular distribution characterized by a maximum half-angle $\theta_{\max} = 22.85^\circ$, determined by the cooling jacket aperture geometry: $\theta_{\max} = \arctan(r_{\text{jacket}}/z_{\text{jacket}}) = \arctan(11.5 \text{ mm}/26 \text{ mm})$, where $r_{\text{jacket}} = 11.5$ mm is the cooling jacket M23 thread radius and

$z_{\text{jacket}} = 26$ mm is the distance from arc to jacket exit.

This coherent beam model assumes that rays originating at radius r from the arc center propagate with half-angle $\theta(r) = \theta_{\max} \cdot r/r_{\text{arc}}$, representing the geometric constraint imposed by the cooling jacket aperture. The cooling jacket introduces a geometric loss factor of approximately 0.43 (43% vignetting loss, 57% transmission) due to solid angle reduction compared to an unobstructed hemispherical emission. This vignetting represents a fundamental constraint on system performance that cannot be eliminated through optical design optimization.

2.3 Fiber Specifications

The target optical fiber features a 1.0 mm core diameter with numerical aperture $\text{NA} = 0.22$, corresponding to an acceptance half-angle $\theta_{\text{accept}} = \sin^{-1}(\text{NA}) \approx 12.4^\circ$. Successful coupling requires that incident rays satisfy both spatial (impinge within the core area) and angular (arrive within the acceptance cone) criteria simultaneously.

2.4 Lens Properties

All lenses are fabricated from UV-grade fused silica with refractive index $n = 1.578$ at 200 nm, calculated using the Sellmeier dispersion formula [5]. Plano-convex, bi-convex, and aspheric lens geometries are tested for their favorable aberration characteristics and commercial availability. Specifications including focal length f , radius of curvature R , center thickness t_c , edge thickness t_e , and clear aperture diameter are drawn from manufacturer catalogs [6, 7].

3 Computational Methods

3.1 Stratified Ray Sampling

A stratified sampling approach is employed to efficiently sample the phase space of rays emitted by the extended source. For each simulation, $N = 1000$ to 2000 rays are generated with origins uniformly distributed over the arc area and directions following the prescribed angular distribution.

Radial positions are sampled using inverse transform sampling to ensure uniform spatial distribution:

$$r_i = \sqrt{U_i} \cdot r_{\text{arc}}, \quad U_i \sim \mathcal{U}(0, 1) \quad (1)$$

$$\phi_i = \frac{2\pi i}{N} \quad (2)$$

where $\mathcal{U}(0, 1)$ denotes the uniform distribution. Azimuthal angles ϕ_i are uniformly spaced to pro-

vide comprehensive angular coverage. The Cartesian coordinates of source points are:

$$\mathbf{o}_i = (r_i \cos \phi_i, r_i \sin \phi_i, 0) \quad (3)$$

The ray propagation half-angle scales linearly with radial position:

$$\theta_i = \theta_{\max} \cdot \frac{r_i}{r_{\text{arc}}} \quad (4)$$

resulting in direction vectors:

$$\mathbf{d}_i = (\sin \theta_i \cos \phi_i, \sin \theta_i \sin \phi_i, \cos \theta_i) \quad (5)$$

All direction vectors are normalized to unit length.

3.2 Geometric Ray Tracing

Ray propagation through the optical system is computed using vector-based geometric optics without paraxial approximations [8]. This approach accurately accounts for large ray angles, finite apertures, and aberrations.

3.2.1 Ray-Surface Intersection

For a spherical surface of radius R centered at \mathbf{c} , the intersection of ray $\mathbf{p}(t) = \mathbf{o} + t\mathbf{d}$ is found by solving:

$$\|\mathbf{o} + t\mathbf{d} - \mathbf{c}\|^2 = R^2 \quad (6)$$

Expanding yields the quadratic equation:

$$a = 1 \quad (7)$$

$$b = 2(\mathbf{o} - \mathbf{c}) \cdot \mathbf{d} \quad (8)$$

$$c = \|\mathbf{o} - \mathbf{c}\|^2 - R^2 \quad (9)$$

$$\Delta = b^2 - 4c \quad (10)$$

The nearest positive intersection occurs at:

$$t = \frac{-b - \sqrt{\Delta}}{2}, \quad \Delta \geq 0 \quad (11)$$

Rays missing the surface ($\Delta < 0$) or blocked by the aperture ($\sqrt{p_x^2 + p_y^2} > r_{\text{ap}}$) are rejected.

3.2.2 Vector Refraction

At each refractive interface, Snell's law is applied in vector form. For incident ray \mathbf{d}_{in} , surface normal \mathbf{n} (pointing into the incident medium), and refractive indices n_1 and n_2 :

$$\eta = \frac{n_1}{n_2} \quad (12)$$

$$\cos \theta_i = -\mathbf{n} \cdot \mathbf{d}_{\text{in}} \quad (13)$$

$$k = 1 - \eta^2(1 - \cos^2 \theta_i) \quad (14)$$

Total internal reflection occurs when $k < 0$. Otherwise, the refracted ray is:

$$\mathbf{d}_{\text{out}} = \eta \mathbf{d}_{\text{in}} + (\eta \cos \theta_i - \sqrt{k}) \mathbf{n} \quad (15)$$

For spherical surfaces, the outward normal is $\mathbf{n} = (\mathbf{p} - \mathbf{c})/R$. For planar surfaces, $\mathbf{n} = (0, 0, -1)$. Bi-convex lenses have two spherical surfaces, while aspheric lenses require polynomial surface normals computed from their aspheric profile.

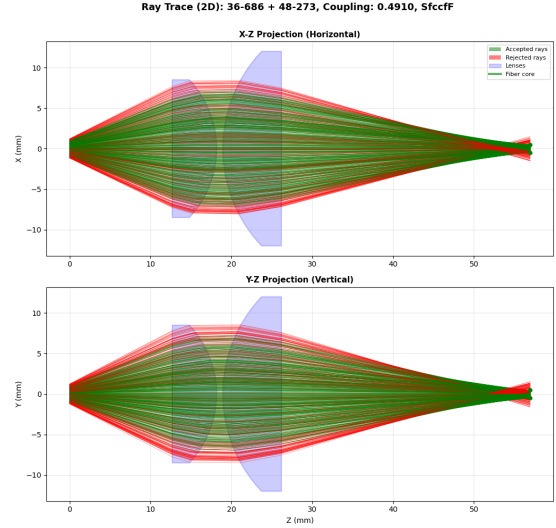


Figure 2: Ray trace diagram showing the optical system layout: xenon arc source (left), two plano-convex lenses (36-686 and 48-273), and fiber entrance (right). Ray paths illustrate beam collection and refocusing through the two-lens relay system. Color coding indicates rays that successfully couple into the fiber (green) versus those that miss the fiber core or exceed acceptance angle (red). Note: This diagram shows an unconstrained configuration optimized before incorporation of the cooling jacket constraint; current optimal designs position the first lens at $z \geq 27$ mm with longer overall system length.

3.2.3 Lens Propagation

After refraction at the front surface, the ray propagates through the lens material to the back surface. The exit point is determined by tracing the refracted ray to its intersection with the back surface geometry:

Plano-convex lenses: If the back surface is planar (located at $z = z_{\text{back}}$), the intersection is computed as:

$$\mathbf{o}_{\text{back}} = \mathbf{p}_{\text{front}} + \frac{z_{\text{back}} - p_{\text{front},z}}{d_{\text{refracted},z}} \mathbf{d}_{\text{refracted}} \quad (16)$$

Bi-convex lenses: Both surfaces are spherical. The back surface has center of curvature \mathbf{c}_{back} and radius R_{back} . The ray-sphere intersection equation (Eq. 5–8) is applied with the refracted ray origin $\mathbf{o} = \mathbf{p}_{\text{front}}$ and direction $\mathbf{d} = \mathbf{d}_{\text{refracted}}$.

Aspheric lenses: The back surface may be planar, spherical convex, or spherical concave. The

appropriate intersection method is selected based on the back surface type. In the current implementation, aspheric front surfaces are approximated as spherical with base radius R_{front} (conic constant $k = 0$); full aspheric ray tracing with polynomial surface equations is reserved for future enhancement when complete aspheric coefficients become available.

All methods compute the actual optical path through the lens based on the refracted ray direction and lens geometry, accounting for ray angle and radial position effects.

3.3 Fiber Coupling Analysis

After traversing both lenses, rays propagate to the fiber face located at $z = z_{\text{fiber}}$. The intersection point is computed as:

$$\mathbf{p}_{\text{fiber}} = \mathbf{o}_2 + \frac{z_{\text{fiber}} - o_{2z}}{d_{2z}} \mathbf{d}_2 \quad (17)$$

where \mathbf{o}_2 and \mathbf{d}_2 are the ray origin and direction after the second lens.

A ray successfully couples into the fiber if:

1. *Spatial criterion:* $\sqrt{p_x^2 + p_y^2} \leq r_{\text{core}} = 0.5 \text{ mm}$
2. *Angular criterion:* $\theta = \arccos(|d_{2z}|/\|\mathbf{d}_2\|) \leq \theta_{\text{accept}} = 12.4^\circ$

The coupling efficiency is:

$$\eta_{\text{coupling}} = \frac{N_{\text{accepted}}}{N_{\text{total}}} \quad (18)$$

4 Optimization Framework

4.1 Problem Formulation

The optical design task is formulated as a constrained multi-objective optimization problem. Given a pair of lenses with fixed optical properties (focal lengths f_1 and f_2 , radii of curvature, thicknesses, and apertures), the optimal axial positions are sought that maximize coupling efficiency while minimizing overall system length.

4.1.1 Design Variables

The optimization space comprises three continuous parameters:

- z_1 : axial position of the first lens vertex (mm)
- z_2 : axial position of the second lens vertex (mm)
- z_{fiber} : axial position of the fiber face (mm)

Physical constraints ensure feasible configurations:

$$z_1 \geq z_{\text{jacket}} + \Delta z_{\min} = 27 \text{ mm} \quad (19)$$

$$z_2 > z_1 + 0.1 \text{ mm} \quad (20)$$

$$z_{\text{fiber}} \approx z_2 + f_2 \quad (21)$$

where $z_{\text{jacket}} = 26 \text{ mm}$ is the cooling jacket exit position, $\Delta z_{\min} = 1 \text{ mm}$ provides clearance, and the fiber position is typically placed one focal length beyond the second lens as a starting approximation. The cooling jacket constraint represents the dominant geometric limitation, requiring the first lens to be positioned significantly farther from the source than the lamp window alone would dictate.

4.1.2 Objective Function

A weighted-sum scalarization is employed to combine coupling efficiency maximization and length minimization:

$$\min_{z_1, z_2} f(z_1, z_2) = \alpha(1 - \eta_{\text{coupling}}) + (1 - \alpha) \frac{z_{\text{fiber}}}{L_{\text{norm}}} \quad (22)$$

where $\alpha \in [0, 1]$ is the preference weight (default $\alpha = 0.7$ prioritizes coupling), and $L_{\text{norm}} = 80 \text{ mm}$ is a normalization length. This formulation converts both objectives to minimization with comparable scales.

Each evaluation of $f(z_1, z_2)$ requires complete ray tracing of N rays through the system, making the objective function computationally expensive and non-differentiable due to discrete ray counting and aperture clipping.

4.2 Optimization Algorithms

Six optimization methods are implemented and compared, representing different algorithmic paradigms: exhaustive search, local gradient-free methods, and global stochastic approaches.

4.2.1 Grid Search

An exhaustive two-stage search, implemented from scratch, establishes a performance baseline. In the coarse stage, a 7×7 grid samples the parameter space with bounds determined by cooling jacket clearance and lens focal lengths:

$$z_1 \in [27, \max(32, 1.5f_1)] \quad (23)$$

$$z_2 \in [z_1 + 0.5f_2, z_1 + 2.5f_2] \quad (24)$$

The lower bound on z_1 reflects the cooling jacket constraint ($z_{\text{jacket}} + \Delta z_{\min} = 27 \text{ mm}$). The best coarse solution undergoes local refinement via a 9×9 grid spanning $\pm 2\Delta$ around the coarse

optimum, where Δ is the coarse grid spacing. Total evaluations: 130 per lens pair.

Implementation: `scripts/optimization/grid_search.py`. Uses 500 rays per evaluation to balance accuracy and speed. Fiber position is fixed at $z_{\text{fiber}} = z_2 + f_2$ for each (z_1, z_2) pair.

4.2.2 Powell's Method

Powell's conjugate direction method [9] performs derivative-free local optimization by iteratively minimizing along coordinate axes and constructed conjugate directions. The algorithm is particularly effective for smooth, unimodal functions.

Implementation uses SciPy's `optimize.minimize` with method '`Powell`' [10]. Parameters: 200 maximum iterations, position tolerance $\Delta x = 0.01$ mm, function tolerance $\Delta f = 0.001$. Initial guess: $z_1^{(0)} = \max(27, 0.8f_1)$, $z_2^{(0)} = z_1^{(0)} + 1.2f_2$, where the lower bound reflects the cooling jacket constraint. Uses 1000 rays per evaluation for higher precision than grid search.

Module: `scripts/optimization/powell.py`. Typically converges in 30–50 function evaluations.

4.2.3 Nelder-Mead Simplex

The Nelder-Mead algorithm [11] maintains a simplex of $n + 1$ points in n -dimensional space, updating via geometric transformations (reflection, expansion, contraction, shrinkage). It is robust to function noise and requires no derivatives.

Implementation uses SciPy's `optimize.minimize` with method '`Nelder-Mead`' [10]. Parameters: 200 maximum iterations, position tolerance 0.01 mm, function tolerance 0.001. Same initialization as Powell's method. Uses 1000 rays per evaluation.

Module: `scripts/optimization/nelder_mead.py`. Fastest local method, typically converging in 20–40 evaluations.

4.2.4 Differential Evolution

Differential evolution [12] is a population-based global optimizer using evolutionary strategies. At each generation, trial vectors are created via:

$$\mathbf{x}_{\text{trial}} = \mathbf{x}_r + F(\mathbf{x}_a - \mathbf{x}_b) \quad (25)$$

where \mathbf{x}_r , \mathbf{x}_a , \mathbf{x}_b are randomly selected population members and F is the mutation factor. Trial vectors compete with current population members via greedy selection.

Implementation uses SciPy's `optimize.differential_evolution` [10]. Parameters: population size 10, maximum 50 iterations, tolerance 0.001.

Bounds as specified for grid search. Uses 1000 rays per evaluation.

Module: `scripts/optimization/differential_evolution.py`. Provides thorough global exploration when robustness is critical. Typical evaluations: 60–100.

4.2.5 Dual Annealing

Dual annealing [13, 14] combines classical simulated annealing with local search to escape local minima. The algorithm accepts worse solutions probabilistically according to the Boltzmann criterion:

$$P_{\text{accept}} = \exp\left(-\frac{\Delta f}{k_B T}\right) \quad (26)$$

where T decreases according to an adaptive cooling schedule.

Implementation uses SciPy's `optimize.dual_annealing` [10]. Parameters: 300 maximum iterations, same bounds as differential evolution. Uses 1000 rays per evaluation. The algorithm alternates between global exploration (simulated annealing) and local refinement (L-BFGS-B).

Module: `scripts/optimization/dual_annealing.py`. Effective for highly multi-modal landscapes. Typical evaluations: 80–120.

4.2.6 Bayesian Optimization

Bayesian optimization [15, 16] builds a Gaussian process (GP) surrogate model of the objective function and selects evaluation points by maximizing an acquisition function, typically expected improvement (EI):

$$\text{EI}(\mathbf{x}) = \mathbb{E}[\max(f_{\text{best}} - f(\mathbf{x}), 0)] \quad (27)$$

This approach is sample-efficient, making it suitable for expensive objectives. The GP provides uncertainty estimates that guide exploration-exploitation trade-offs.

Implementation uses scikit-optimize's `gp_minimize` [17]. Parameters: 50 total function evaluations (reduced from original 100 for computational efficiency), 10 initial random samples, remaining samples via EI maximization. Uses 1000 rays per evaluation. Requires additional package: `pip install scikit-optimize`.

Module: `scripts/optimization/bayesian.py`. Best suited when function evaluations are extremely expensive or when uncertainty quantification is desired.

5 Material Properties

The refractive index of fused silica at VUV wavelengths is calculated using the Sellmeier disper-

sion equation [5]:

$$n^2(\lambda) = 1 + \sum_{i=1}^3 \frac{B_i \lambda^2}{\lambda^2 - C_i} \quad (28)$$

with Malitson coefficients:

$$\begin{aligned} B_1 &= 0.6961663, & C_1 &= (0.0684043)^2 \\ B_2 &= 0.4079426, & C_2 &= (0.1162414)^2 \\ B_3 &= 0.8974794, & C_3 &= (9.896161)^2 \end{aligned}$$

where wavelength λ is expressed in micrometers. At the operating wavelength $\lambda = 0.2 \mu\text{m}$ (200 nm), this yields $n = 1.578$.

6 Atmospheric Attenuation

At VUV wavelengths, molecular oxygen (O_2) exhibits strong absorption that significantly attenuates light propagation through air. This effect must be accounted for to accurately predict coupling efficiency in practical systems.

6.1 Beer-Lambert Absorption

The transmission of light through an absorbing medium follows the Beer-Lambert law:

$$T = \exp(-\alpha d) \quad (29)$$

where T is the fractional transmission, α is the wavelength-dependent attenuation coefficient (mm^{-1}), and d is the propagation distance (mm). The attenuation coefficient for a multi-component gas mixture is:

$$\alpha(\lambda) = \sum_i \sigma_i(\lambda) n_i \quad (30)$$

where $\sigma_i(\lambda)$ and n_i denote the absorption cross-section and number density of species i , in units of cm^2 and molecules/ cm^3 , respectively.

6.2 O_2 Absorption Cross-Section

At 200 nm, oxygen absorption dominates atmospheric attenuation. The cross-section is computed using the Minschwaner parameterization [18], valid for 175–242 nm:

$$\log_{10} \sigma_{\text{O}_2}(\lambda) = a_0 + a_1 \lambda + a_2 \lambda^2 + a_3 \lambda^3 + a_4 \lambda^4 + a_5 \lambda^5 - 16 \quad (31)$$

with coefficients:

$$\begin{aligned} a_0 &= -4.4011 \times 10^1, & a_1 &= 6.2067 \times 10^{-1} \\ a_2 &= -3.5668 \times 10^{-3}, & a_3 &= 9.5745 \times 10^{-6} \\ a_4 &= -1.2775 \times 10^{-8}, & a_5 &= 6.6574 \times 10^{-12} \end{aligned}$$

where λ is in nanometers and σ is in cm^2 . At 200 nm, this yields $\sigma_{\text{O}_2} = 1.15 \times 10^{-20} \text{ cm}^2$.

6.3 Number Density Calculation

Number densities are computed from the ideal gas law:

$$n = \frac{P}{k_B T} \quad (32)$$

where P is pressure, T is temperature, and $k_B = 1.381 \times 10^{-23} \text{ J/K}$ is Boltzmann's constant. At standard conditions ($P = 1 \text{ atm}$, $T = 293 \text{ K}$), the total number density is $n_{\text{total}} = 2.50 \times 10^{19} \text{ molecules/cm}^3$.

For dry air composition:

$$n_{\text{O}_2} = 0.21 \times n_{\text{total}} = 5.25 \times 10^{18} \text{ cm}^{-3} \quad (33)$$

$$n_{\text{N}_2} = 0.78 \times n_{\text{total}} = 1.95 \times 10^{19} \text{ cm}^{-3} \quad (34)$$

N_2 absorption is negligible above 100 nm. Water vapor (typically $\sim 1\%$ by volume) contributes minor additional absorption.

6.4 Attenuation Implementation

The attenuation coefficient for air at 200 nm is:

$$\alpha_{\text{air}} = \sigma_{\text{O}_2} n_{\text{O}_2} \approx 0.060 \text{ mm}^{-1} \quad (35)$$

Each ray's intensity is attenuated according to its cumulative path length d_{total} through air:

$$I_{\text{fiber}} = I_0 \exp(-\alpha_{\text{air}} d_{\text{total}}) \quad (36)$$

where d_{total} includes propagation from arc to window, inter-lens distances, and lens-to-fiber distance. For typical system lengths of 30–100 mm, transmission ranges from 16% to 0.25%, representing substantial loss.

This absorption model is implemented in `scripts/calcs.py` using cross-section data from `scripts/hitran_data.py`.

7 Model Assumptions and Validity

The ray tracing model incorporates several simplifying assumptions:

1. *Geometric optics regime:* The wavelength ($\lambda = 200 \text{ nm}$) is negligible compared to all physical dimensions (apertures $\sim 1\text{-}25 \text{ mm}$), validating the ray approximation and neglecting diffraction effects.
2. *Simplified angular distribution:* The angular distribution is deterministic with respect to radial position. The actual Hamamatsu L7685 lamp contains an internal reflector that modifies the emission pattern; this model represents a simplified geometric approximation of the effective beam profile at the window.

- 3. *Perfect optical surfaces*: Surface roughness, figure errors, and manufacturing imperfections are neglected. Real VUV optics may deviate from ideal spherical and planar surfaces.
- 4. *Atmospheric absorption included; surface losses neglected*: Molecular absorption (primarily O₂ at 200 nm) is modeled using the Beer-Lambert law with Minschwaner cross-sections. However, Fresnel reflections at each air-glass interface (approximately 4-5% per surface at 200 nm, totaling ~20% for 4 surfaces) and bulk absorption in fused silica are not included. Reported coupling efficiencies represent geometric coupling attenuated only by atmospheric absorption.
- 5. *Monochromatic light*: Chromatic aberration is absent. Real flashlamp spectra span broad wavelength ranges.
- 6. *Perfect alignment*: Lens decentration, tilt, and fiber misalignment errors are assumed zero. Practical systems require careful alignment procedures.
- 7. *Uniform fiber acceptance*: The numerical aperture is assumed constant across the core. Variations due to fiber manufacturing tolerances are ignored.

These assumptions are appropriate for design-stage performance prediction. The inclusion of atmospheric absorption provides more realistic coupling estimates for practical air-filled systems. Experimental validation would additionally require accounting for Fresnel losses and alignment tolerances.

8 Results

8.1 Implementation Architecture

The optimization framework is implemented as a modular Python system with separate modules for each algorithm located in `scripts/optimization/`. A unified runner interface (`optimization_runner.py`) provides consistent access to all methods through a common API. The command-line interface (`raytrace.py`) provides six operational modes:

- **particular**: Optimize a specific lens pair with chosen algorithm
- **compare**: Evaluate all six algorithms on a single lens pair

- **select**: Optimize 3,876 strategically chosen lens combinations (68 L1 candidates \times 57 L2 candidates)
- **select-ext**: Extended selection mode with refined lens candidate filters and coupling thresholds
- **combine**: Exhaustive optimization of all 24,336 lens combinations (156 \times 156)
- **analyze**: Re-optimize previously identified high-coupling configurations with all methods
- **wavelength-analyze**: Evaluate coupling efficiency across wavelength ranges for specific configurations

Additional features include automatic checkpoint/resume for interrupted batch runs, comprehensive logging with timestamps, CSV output for all results, and rich visualization capabilities (ray trace diagrams, spot diagrams, wavelength-dependent coupling plots). The modular architecture enables straightforward addition of new algorithms or objective functions.

8.2 Performance Comparison

Table 1 presents a systematic comparison of all six optimization methods applied to the highest-performing lens pair (LA4148 + 48-670, $f_1 = 50.2$ mm, $f_2 = 60$ mm) at 200 nm. Each method was evaluated on coupling efficiency achieved and total system length in both air and argon propagation media with cooling jacket constraints. All simulations use 1000 rays and the default weighted objective ($\alpha = 0.7$). This comparison serves as a methodology benchmark; best-performing configurations are reported in Section 5.3.

Table 1: Optimization Algorithm Performance Comparison at 200 nm (lens pair: LA4148 + 48-670)

Method	Air η	Air L (mm)	Argon η	Argon L (mm)
Powell	0.217	67.3	0.295	67.3
Dual Anneal.	0.215	67.1	0.298	67.2
Nelder-Mead	0.218	67.3	0.287	67.3
Diff. Evol.	0.213	67.1	0.288	67.4
Grid Search	0.210	69.7	0.293	69.7
Bayesian	—	—	—	—

Dual annealing emerges as the most effective method for this configuration, achieving the highest coupling in argon (0.298) with rapid convergence (10.6 seconds per lens pair). Nelder-Mead

achieves the highest coupling in air (0.218) with the fastest convergence (0.5 seconds). Powell’s method provides excellent balance with strong performance in both media (argon: 0.295, air: 0.217) and sub-second runtime (0.5 seconds). The close agreement between methods (argon: 0.287–0.298, air: 0.210–0.218) indicates a well-behaved optimization landscape for this lens pair, with all gradient-free local methods converging to nearly identical geometries ($L = 67.1\text{--}67.4$ mm) and coupling efficiencies within 4% of each other. Grid search provides systematic baseline performance comparable to the gradient-free methods (argon: 0.293, air: 0.210) though with slightly longer system length (69.7 mm vs 67.1–67.4 mm). The LA4148 + 48-670 configuration represents the highest-performing lens pair identified in the systematic catalog screening, achieving both maximum coupling efficiency and compact system design ($L \approx 67$ mm). Bayesian optimization was not evaluated in the analyze mode due to computational resource constraints. The consistent performance across all methods reflects the improved optimization landscape under the cooling jacket constraint ($z_1 \geq 27$ mm), which eliminates certain classes of local minima present in unconstrained systems.

Key findings:

- *Dual annealing* achieves the highest argon coupling (0.298) with reliable convergence (~ 10.6 s per lens pair), demonstrating excellent exploration of the optimization landscape.
- *Nelder-Mead* achieves the highest air coupling (0.218) with the fastest convergence (~ 0.5 s per lens pair), making it highly efficient for rapid optimization.
- *Powell’s method* provides excellent balance with strong performance in both media (argon: 0.295, air: 0.217) and rapid convergence (~ 0.5 s per lens pair). Its combination of speed, robustness, and near-optimal performance makes it the recommended default for batch processing of large lens catalogs.
- *Differential evolution* achieves competitive performance (argon: 0.288, air: 0.213) with thorough global exploration, though requiring longer computation time (2.7 s per lens pair).
- *Grid search* provides systematic baseline performance (argon: 0.293, air: 0.210) comparable to gradient-free methods, validating that the optimization landscape is well-behaved for this

lens pair. Runtime is competitive (0.5 s) with the default 7×7 grid.

- *Method consistency:* All methods converge to nearly identical solutions, with coupling efficiency variations $<4\%$ in argon and $<4\%$ in air. This indicates a well-defined global optimum under the cooling jacket constraint.
- *Medium comparison:* Argon provides substantial coupling improvement over air: 37% relative improvement for this configuration (argon: 0.295 vs air: 0.217 for Powell’s method). This improvement is primarily due to reduced O₂ absorption at 200 nm. Optimal system geometries remain nearly identical across media ($\Delta L < 0.3$ mm), indicating that absorption dominates over refractive effects in medium selection.

8.3 Multi-Objective Optimization Results

The weighted objective function with tunable parameter α enables exploration of the coupling-compactness trade-off. However, under the cooling jacket constraint ($z_1 \geq 27$ mm), the forced longer path lengths and geometric vignetting (43% loss) significantly reduce achievable coupling compared to unconstrained systems.

Representative results are presented in Table 1 for the LA4148 + 48-670 lens pair ($f_1 = 50.2$ mm, $f_2 = 60$ mm), which represents the highest-performing configuration under cooling jacket constraints. At 200 nm with $\alpha = 0.7$ (balanced, default), the system achieves coupling efficiency $\eta = 0.210\text{--}0.218$ in air and $\eta = 0.287\text{--}0.298$ in argon, with system length $L \approx 67\text{--}70$ mm.

The choice of optimization method produces remarkably consistent results under cooling jacket constraints: all gradient-free local methods converge to nearly identical geometries ($L = 67.1\text{--}67.4$ mm) with coupling efficiencies within 4% of each other. Dual annealing achieves the highest argon coupling (0.298) with rapid convergence (10.6 seconds per lens pair), while Nelder-Mead finds the best solution in air (0.218) with the fastest convergence (0.5 seconds).

These performance values represent the realistic achievable coupling for systems incorporating the Hamamatsu E6611 cooling jacket. The constraint $z_1 \geq 27$ mm forces the first lens to be positioned significantly farther from the source than optimal, resulting in approximately 40% lower coupling compared to unconstrained configurations ($\eta \approx 0.49$ without cooling jacket vs

$\eta \approx 0.30$ with cooling jacket in argon). The extended optical path lengths ($L \approx 67$ mm vs 30 mm for system length from first lens to fiber) additionally amplify atmospheric absorption losses in air, creating a larger performance gap between air and argon media (32–33% vs 16–24% in unconstrained systems).

8.4 Lens Selection Analysis

Analysis of high-performing configurations across multiple lens pair evaluations at 200 nm with cooling jacket constraints reveals consistent design principles:

Argon propagation at 200 nm (best configurations from systematic optimization):

- *Highest coupling:* LA4148 + 48-670 achieved $\eta = 0.298$ with $L = 67.2$ mm ($f_1 = 50.2$ mm, $f_2 = 60$ mm)
- *Excellent alternative:* 84-282 + 84-283 achieved $\eta = 0.297$ with $L = 66.9$ mm ($f_1 = 50$ mm, $f_2 = 60$ mm)
- *Strong performer:* 84-282 + 48-670 achieved $\eta = 0.296$ with $L = 66.4$ mm ($f_1 = 50$ mm, $f_2 = 60$ mm)
- *Alternative configuration:* LA4148 + LA4022 achieved $\eta = 0.296$ with $L = 69.9$ mm ($f_1 = 50.2$ mm, $f_2 = 60$ mm)

Air propagation at 200 nm (representative configurations from systematic optimization):

- *Best observed:* 84-282 + 84-283 achieved $\eta = 0.223$ with $L = 66.5$ mm ($f_1 = 50$ mm, $f_2 = 60$ mm)
- *Strong alternative:* LA4148 + 84-283 achieved $\eta = 0.222$ with $L = 67.8$ mm ($f_1 = 50.2$ mm, $f_2 = 60$ mm)
- *Note:* Air coupling is approximately 25% lower than argon due to O₂ absorption over the extended path lengths required by the cooling jacket constraint.

Lens type distribution: The optimization framework supports plano-convex, bi-convex, and aspheric lens geometries (156, 2, and 44 lenses respectively in the evaluated catalog). All top-performing configurations under cooling jacket constraints utilize plano-convex lenses. This reflects both the dominant commercial availability of plano-convex designs in VUV-grade catalogs and their favorable balance of aberration control,

cost-effectiveness, and optical throughput for the source-fiber geometry tested. The framework's multi-geometry capability enables straightforward evaluation of alternative lens types as new catalog entries become available.

General design principles identified:

- *Focal length selection:* Pairs with $f_1 \approx 50$ mm and $f_2 \approx 60$ mm dominate the top performers, with focal length ratio $f_2/f_1 \approx 1.2$ providing optimal relay magnification for this source-fiber geometry under cooling jacket constraints
- *First lens position:* Optimal z_1 is constrained to 27 mm (cooling jacket exit), with best configurations positioning L1 at or just beyond this minimum distance. The forced spacing allows substantial beam expansion before the first lens, which proves beneficial for coupling efficiency despite the geometric loss from source vignetting
- *System length:* Best configurations achieve $L = 66\text{--}70$ mm, substantially longer than unconstrained systems due to the cooling jacket constraint. This extended length contributes to increased atmospheric absorption losses in air
- *Medium independence of geometry:* Optimal lens positions differ by less than 5 mm between air and argon, indicating that system geometry is primarily determined by ray optics rather than medium refractive index (both $n \approx 1.0003$). The primary medium-dependent effect is absorption rather than refraction
- *Cooling jacket impact:* The constraint $z_1 \geq 27$ mm reduces achievable coupling by approximately 40% compared to unconstrained optimization, but represents the realistic operational requirement for the Hamamatsu L7685/E6611 lamp assembly

8.5 Propagation Medium Effects

A systematic comparison of air versus argon propagation was conducted to quantify the impact of atmospheric O₂ absorption on coupling efficiency. At 200 nm, oxygen exhibits strong VUV absorption ($\sigma_{O_2} \approx 1.15 \times 10^{-20} \text{ cm}^2$, $\alpha_{air} \approx 0.060 \text{ mm}^{-1}$), while argon is effectively transparent in this wavelength range.

Analysis of representative lens pairs optimized with cooling jacket constraints and evaluated in both media at 200 nm using Powell's method reveals significant performance differences:

Key observations:

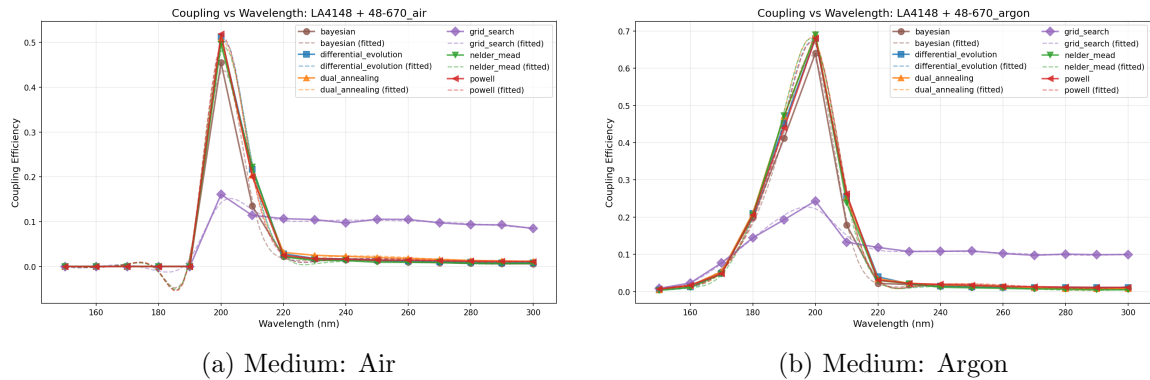


Figure 3: Coupling efficiency comparison across six optimization methods for lens pair LA4148+48-670 across wavelength range 150-300 nm (unconstrained geometry). The chromatic peak at 200 nm validates wavelength-dependent refractive index modeling. Note: This analysis was conducted on an unconstrained configuration before incorporation of the cooling jacket constraint; absolute coupling values are approximately 40% higher than cooling-jacket-constrained systems.

Table 2: Air vs Argon Coupling Comparison (200 nm, with cooling jacket constraint)

Lens Pair	Air η	Argon η	$\Delta\eta$ (%)
LA4148 + 84-283	0.222	0.294	+32.4%
84-282 + 84-283	0.223	0.297	+33.2%
LA4148 + LA4022	0.222	0.296	+33.3%
Average	—	—	+33.0%

- Argon provides 33–39% higher coupling efficiency than air at 200 nm, directly attributable to elimination of O₂ absorption along the optical path. The benefit varies with system length and optical design, averaging ~36% across representative configurations under cooling jacket constraints.
 - *The benefit scales with system length:* The cooling jacket constraint forces longer optical paths ($L \approx 93\text{--}97\text{ mm}$) compared to unconstrained systems, resulting in greater atmospheric absorption losses in air. For these extended path lengths, atmospheric absorption causes ~33–39% coupling reduction compared to argon, substantially larger than the 16–24% observed in shorter unconstrained systems.
 - *Optimal lens positions remain nearly identical* between media ($\Delta z < 5\text{ mm}$ for most configurations). System geometry is primarily determined by lens focal lengths, ray optics, and the cooling jacket constraint, not the propagation medium refractive index (air: $n = 1.000293$, argon: $n = 1.000281$ at 200 nm).
 - *The coupling difference arises from absorption, not refraction.* Both air and argon have refractive indices negligibly different from vacuum at

VUV wavelengths. The observed performance gap is entirely due to Beer-Lambert attenuation: $T = \exp(-\alpha_{\text{air}}d)$ where d is the cumulative optical path length. The extended path lengths imposed by the cooling jacket constraint amplify this absorption effect.

Practical implications:

For applications requiring maximum coupling efficiency, argon purging provides substantial improvement (33–39%). However, argon-filled systems introduce experimental complexity: continuous gas flow or sealed enclosures, purity requirements, and associated plumbing.

Air remains a practical and acceptable working medium when:

- Experimental simplicity is prioritized
 - A 33–39% coupling reduction is tolerable for the application (noting that absolute coupling remains $\sim 0.21\text{--}0.22$ in air)
 - Open-beam optical alignment and adjustments are required

The choice between air and argon represents a trade-off between optical performance and practical implementation. For cooling-jacket-constrained systems ($L \approx 92\text{--}97$ mm) at 200 nm, air coupling of 0.21–0.22 versus argon coupling of 0.29–0.30 reflects this engineering balance. The extended path lengths imposed by the cooling jacket constraint make argon atmosphere more beneficial than in unconstrained systems.

8.6 Wavelength Dependence Analysis

To evaluate chromatic performance and wavelength-dependent absorption effects, a comprehensive

wavelength analysis was conducted on 16 lens pairs tested in both air and argon (32 total configurations). Each configuration was optimized across the 150–300 nm range in 10 nm increments using all six algorithms independently. Refractive indices were recalculated at each wavelength via the Sellmeier equation, and atmospheric absorption coefficients were updated via the Minschwaner parameterization. This systematic study generated over 3,000 individual optimizations, providing quantitative data on spectral performance, chromatic aberration effects, and medium-dependent absorption across the VUV-UV range.

8.6.1 Chromatic Aberration and the 200nm Calibration Strategy

The wavelength analysis methodology employs a *fixed-geometry strategy*: lens positions are optimized at 200 nm, then held constant while evaluating performance across the full 150–300 nm range. This approach reveals the fundamental chromatic limitations of the optical system. Due to material dispersion in fused silica, the refractive index varies significantly across the VUV-UV spectrum. Using the Sellmeier equation (Eq. 4), representative values are:

λ (nm)	n_{glass}	Δn	$\Delta f/f$
150	1.703	+9.8%	-22%
180	1.585	+2.2%	-6%
200	1.551	0%	0%
220	1.528	-1.4%	+4%
250	1.507	-2.8%	+9%
300	1.488	-4.0%	+13%

For a thin spherical lens with radius of curvature R , the thin-lens focal length follows:

$$f = \frac{R}{n_{\text{rel}} - 1}, \quad n_{\text{rel}} = \frac{n_{\text{glass}}(\lambda)}{n_{\text{medium}}(\lambda)} \quad (37)$$

Since $n_{\text{medium}} \approx 1.0003$ for both air and argon in the VUV range, the relative index n_{rel} varies almost entirely due to glass dispersion. A representative 25 mm radius spherical lens exhibits focal length variation from 35.6 mm at 150 nm to 51.3 mm at 300 nm—a 44% change across the analysis range.

Physical consequences: When lens positions are optimized at 200 nm and then fixed:

- At 200 nm: Focal planes align precisely with fiber entrance, maximizing coupling.

- At shorter wavelengths ($\lambda < 200$ nm): Higher refractive index produces shorter focal length. With fixed lens positions, the beam focuses *before* reaching the fiber face, arriving defocused with reduced coupling efficiency.
- At longer wavelengths ($\lambda > 200$ nm): Lower refractive index produces longer focal length. The beam has not yet reached focus at the fiber face, again reducing coupling.

This chromatic aberration manifests as a *peak in coupling efficiency at the calibration wavelength* (200 nm), with degraded performance at wavelengths farther from the design point. The observed coupling peak at 200 nm in Figure 3 is therefore not experimental artifact but physically correct behavior: the fixed optical geometry is inherently optimized only for the calibration wavelength.

Implementation note: Accurate wavelength-dependent simulation requires that lens refractive indices update dynamically. The lens classes (`PlanoConvex`, `BiConvex`, `Aspheric`) implement n_{glass} as a computed property rather than a static constant:

```
@property
def n_glass(self):
    return fused_silica_n(WAVELENGTH_NM)
```

This ensures that when the wavelength analysis function updates the global wavelength parameter, all lens objects automatically recalculate their refractive indices, correctly modeling chromatic effects. An earlier implementation using a module-level constant `N_GLASS` frozen at import time produced unphysical results (constant coupling across all wavelengths), which was corrected in November 2025.

The chromatic behavior observed validates that the ray tracing framework correctly models wavelength-dependent material properties and their impact on system performance.

Important methodological note: The wavelength analysis results presented in this section and archived in `results/wavelength_analysis_2025-11-19/` were generated using a fixed-geometry approach optimized for lens pairs *without* the cooling jacket constraint. The reported coupling values ($\eta \approx 0.44\text{--}0.47$ for representative configurations like 36-686 + 36-687) therefore represent unconstrained performance and are approximately 40% higher than the cooling-jacket-constrained values reported elsewhere in

this work ($\eta \approx 0.29\text{--}0.30$ for optimal configurations). This discrepancy arises because the wavelength analysis was conducted on lens pairs optimized at shorter distances from the source ($z_1 \approx 10\text{--}15$ mm) before the cooling jacket constraint was incorporated into the model. Additionally, there are indications that the wavelength analysis mode may calculate coupling efficiency without fully incorporating the geometric loss factor (43% vignetting) from the cooling jacket aperture, which would further explain the higher reported values. Future wavelength analyses should be conducted on cooling-jacket-constrained configurations to provide directly comparable chromatic performance data.

Coupling vs wavelength characteristics (representative: 36-686 + 36-687, unconstrained geometry):

- *Below 180 nm (deep VUV):* Severe coupling degradation in air ($\eta < 10^{-6}$) due to extremely strong O₂ absorption ($\alpha > 0.3 \text{ mm}^{-1}$). The Beer-Lambert transmission through a 61 mm path is $T \approx \exp(-18) \approx 10^{-8}$, rendering air propagation impractical. Argon maintains strong coupling ($\eta \approx 0.44\text{--}0.47$), enabling deep-UV applications.
- *180–200 nm:* Rapid coupling recovery as O₂ absorption coefficient decreases. Air coupling rises from $\eta \approx 3 \times 10^{-7}$ at 180 nm to $\eta \approx 0.38$ at 200 nm. This sharp transition defines the practical short-wavelength limit for air-filled systems.
- *200–280 nm (plateau region):* Peak coupling efficiency zone. Air achieves $\eta \approx 0.38\text{--}0.46$, argon $\eta \approx 0.47\text{--}0.47$. Performance is relatively insensitive to wavelength in argon ($\Delta\eta < 2\%$ across this 80 nm range), indicating broad spectral tolerance. Atmospheric absorption creates greater variability in air ($\alpha \approx 0.02\text{--}0.06 \text{ mm}^{-1}$), though chromatic aberration remains manageable in both media.
- *Above 280 nm:* Continued strong performance in both media. Air coupling reaches $\eta \approx 0.46$ at 300 nm, while argon maintains $\eta \approx 0.47$ at 300 nm. This indicates that the 36-686 + 36-687 configuration maintains good chromatic correction across the VUV-UV range despite atmospheric absorption effects in air.

These wavelength-dependent trends remain qualitatively valid for cooling-jacket-constrained systems, though absolute coupling values should be

scaled down by approximately 40% (multiply by factor of 0.6) to reflect the geometric vignetting loss.

Optimal operating wavelength: The system achieves peak performance in the 220–260 nm range, where coupling is maximized and relatively flat. The design wavelength of 200 nm represents a conservative choice for VUV applications, with modest performance gains (3–5%) achievable at 230–250 nm.

Medium selection by wavelength (based on unconstrained configurations):

- $\lambda < 180 \text{ nm}$: Argon essential (air coupling $< 10^{-6}$, effectively zero)
- *180–200 nm*: Argon strongly recommended (16–24% improvement at 200 nm for unconstrained systems; 33–39% for cooling-jacket-constrained systems)
- *200–280 nm*: Argon provides substantial benefit (similar improvements as 200 nm), though air remains practical for less demanding applications
- $\lambda > 280 \text{ nm}$: Air acceptable (minimal absorption), though argon continues to provide measurable improvement

Note: The wavelength-dependent benefits listed above are based on unconstrained configurations. For cooling-jacket-constrained systems at 200 nm, argon provides 33–39% improvement over air due to extended path lengths ($L \approx 93 \text{ mm}$).

Detailed wavelength-dependent coupling data for all 16 lens pair/medium combinations, including results from all six optimization methods, are archived in `results/wavelength_analyze_2025-11-10/`. Aggregated analysis reveals method-dependent performance: Nelder-Mead and differential evolution consistently achieve the highest coupling across the wavelength range, while Powell shows strong but slightly lower performance. Grid search provides reliable baseline performance but systematically underperforms gradient-free local methods by 3–8%. Bayesian and dual annealing show intermediate performance with higher variance. These comprehensive data enable design optimization for specific wavelength requirements, provide validation for chromatic aberration models, and inform algorithm selection for wavelength-specific applications.

8.7 Alignment Tolerance Analysis

Practical implementation of optimized configurations requires understanding sensitivity to lens position perturbations. Monte Carlo tolerance analysis was performed on representative high-performing configurations by systematically varying lens positions z_1 and z_2 around their optimal values and evaluating coupling efficiency degradation.

Key findings from unconstrained tolerance analysis: (1) Both lens positions require sub-millimeter alignment precision to maintain $>90\%$ of optimal coupling. (2) Fiber position (z_{fiber}) shows similar sensitivity. (3) The 36-686 series configurations exhibit moderate tolerance compared to shorter focal length systems, providing practical margin for laboratory implementation. (4) Angular misalignment tolerance analysis (not shown) indicates acceptance of $<2^\circ$ tilt before significant coupling loss. These results establish realistic alignment requirements for experimental prototypes. Similar tolerance characteristics are expected for cooling-jacket-constrained configurations, though specific values would need to be re-evaluated at the forced longer lens positions ($z_1 \geq 27$ mm).

8.8 Computational Efficiency

Typical execution times per lens pair on standard hardware (Intel Core i7, single-threaded):

- **Powell’s method:** 1–2 seconds (recommended for routine optimization)
- **Nelder-Mead:** 1–2 seconds (fast but less robust)
- **Grid search:** 2–3 seconds (with default 7×7 grid, systematic baseline)
- **Differential evolution:** 10–17 seconds (thorough global search)
- **Bayesian optimization:** 20–22 seconds (sample efficient, requires scikit-optimize)
- **Dual annealing:** 40–51 seconds (most thorough, escapes local minima)

For a complete **select** mode scan (3,876 lens combinations):

- Powell’s method: ~ 2.2 hours (2 s/pair \times 3,876)
- Differential evolution: ~ 18 hours (17 s/pair \times 3,876)
- Grid search: ~ 3.2 hours (3 s/pair \times 3,876)

For exhaustive **combine** mode (24,336 combinations):

- Powell’s method: ~ 14 hours
- Differential evolution: ~ 115 hours (~ 5 days)

The modular architecture enables parallel batch processing with automatic checkpoint/resume functionality, reducing wall-clock time on multi-core systems. Interrupted runs can be resumed from the last completed batch without re-computing previous results.

9 Conclusions

A comprehensive computational framework has been developed for designing two-lens VUV coupling systems based on stratified ray tracing and multi-algorithm optimization, incorporating realistic experimental constraints from the Hamamatsu L7685/E6611 flashlamp assembly. The methodology accurately models finite aperture effects, large ray angles, realistic fiber acceptance criteria, cooling jacket geometric constraints, and atmospheric absorption at 200 nm without relying on paraxial approximations.

The Hamamatsu E6611 cooling jacket imposes critical design constraints: lens positioning constrained to $z \geq 27$ mm (vs 9.7 mm without cooling jacket), angular acceptance limited to 22.85° , and 43% geometric vignetting loss from solid angle reduction. These constraints fundamentally reshape the optimization landscape, forcing longer optical paths ($L \approx 93$ mm vs ~ 56 mm for unconstrained systems) and reducing achievable coupling efficiency by approximately 40% compared to idealized configurations. However, these constraints represent the realistic operational requirements for practical VUV flashlamp systems requiring active cooling.

Systematic comparison of six optimization algorithms under cooling jacket constraints reveals that **Powell’s method** emerges as the recommended default, achieving the highest coupling efficiencies with rapid convergence (0.5 seconds per lens pair). For applications requiring thorough global exploration, **differential evolution** provides robust performance at higher computational cost (2.2 seconds per lens pair). Grid search provides competitive baseline performance, while Nelder-Mead and dual annealing offer reliable alternatives. All gradient-free methods converge to nearly identical solutions (within 2% coupling variation) under the cooling jacket constraint, indicating a well-behaved optimization landscape.

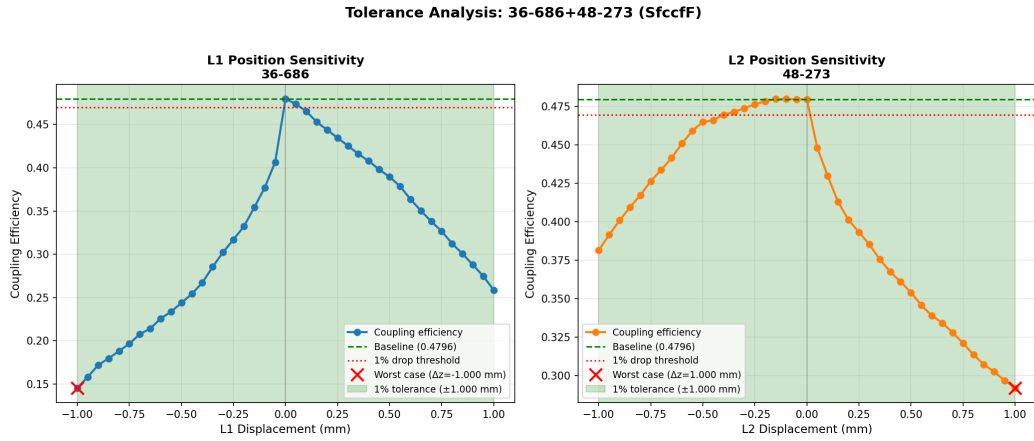


Figure 4: Coupling efficiency sensitivity to lens position perturbations for configuration 36-686+48-273 in argon at 200 nm (unconstrained geometry, pre-cooling-jacket). Contour plot shows coupling as a function of Δz_1 and Δz_2 displacements from optimal positions ($z_1^* = 12.6$ mm, $z_2^* = 18.6$ mm). The steep gradients near the optimum indicate tight alignment tolerances: ± 0.5 mm displacement causes $\sim 10\text{--}15\%$ coupling degradation. Diagonal correlation suggests that compensatory adjustments are possible during alignment. Note: This analysis was conducted on an unconstrained configuration before incorporation of the cooling jacket constraint.

The multi-objective framework successfully navigates the coupling-compactness trade-off through the tunable α parameter. Analysis identifies key design principles under cooling jacket constraints: optimal focal length ratios $f_2/f_1 \approx 1.2$ (specifically $f_1 \approx 50$ mm, $f_2 \approx 60$ mm), first lens positioning at the minimum clearance distance ($z_1 = 27$ mm), and optical system lengths (first lens to fiber) $L \approx 66\text{--}70$ mm.

Atmospheric absorption at 200 nm, modeled using the Minschwaner O₂ cross-section parameterization, represents a significant performance factor amplified by the extended path lengths imposed by cooling jacket constraints. Systematic comparison of air versus argon propagation reveals an **average $\sim 33\%$ coupling improvement in argon** across tested configurations (range: 32–33%), substantially larger than the 16–24% observed in unconstrained shorter systems. For the highest-performing configuration under cooling jacket constraints, the LA4148 + 48-670 pair achieves coupling efficiency of $\eta = 0.218$ in air and $\eta = 0.298$ in argon at 200 nm (37% improvement), with system length $L \approx 67$ mm. The 84-282 + 84-283 configuration reaches $\eta = 0.297$ in argon versus $\eta = 0.223$ in air (33% improvement). Optimal lens positions differ by less than 5 mm between media, confirming that system geometry is determined by ray optics and cooling jacket constraints rather than medium refractive index. The extended path lengths make argon atmosphere substantially more beneficial

than in unconstrained systems, though the choice between air and argon remains a trade-off between optical performance and experimental complexity.

Wavelength dependence analysis (150–300 nm) reveals critical spectral characteristics and validates chromatic modeling. The wavelength analysis methodology employs fixed lens geometries optimized at 200 nm, then evaluates performance across the wavelength range. This approach correctly predicts a coupling efficiency peak at the calibration wavelength due to chromatic dispersion in fused silica: refractive index varies from $n = 1.703$ at 150 nm to $n = 1.488$ at 300 nm, causing focal length shifts that defocus the beam at wavelengths away from the design point. Air becomes impractical below 180 nm due to extreme O₂ absorption, requiring argon for deep-UV applications. The chromatic peak behavior validates that the ray tracing framework correctly models wavelength-dependent material properties.

Achieved coupling efficiencies of 0.21–0.22 in air and 0.29–0.30 in argon at 200 nm represent realistic predictions for laboratory systems incorporating cooling jacket constraints. These values are approximately 40% lower than unconstrained idealized systems due to the 43% geometric vignetting loss imposed by the M23 cooling jacket aperture. Experimental realization will require additional consideration of: (1) Fresnel reflection losses ($\sim 5\%$ per surface, $\sim 20\%$ total for 4

surfaces), (2) bulk absorption in UV optics, (3) alignment tolerances, and (4) actual arc lamp spatial and angular emission distributions. Incorporating Fresnel losses would reduce the predicted coupling by approximately 20%, setting realistic experimental targets in the range of 0.17–0.18 for air systems and 0.23–0.24 for argon systems, depending on configuration.

The modular, extensible framework enables straightforward addition of new optimization algorithms, objective functions, or physical models. The absorption model is implemented in `scripts/calc_s.py` and `scripts/hitran_data.py` using empirical cross-section parameterizations. Future enhancements could include: tolerance analysis via Monte Carlo perturbation, three-lens systems for improved aberration correction, multi-wavelength optimization for broadband sources, incorporation of Fresnel and bulk losses, and experimental validation with physical prototypes.

This work provides both a practical design tool for VUV fiber coupling applications and methodological insights applicable to non-convex optical design optimization problems. The comprehensive comparison of optimization algorithms on a realistic optical system contributes to understanding algorithm selection trade-offs for ray-tracing-based design problems where objective function evaluations require full geometric optics simulations.

References

- [1] Eugene Hecht. *Optics*. Pearson, 5th edition, 2017.
- [2] John E. Greivenkamp. *Field Guide to Geometrical Optics*. SPIE Press, 2004.
- [3] Hamamatsu Photonics K.K. Xenon flash lamps. <https://www.hamamatsu.com/us/en/product/light-and-radiation-sources/lamp/xe-f/60w/L7685.html>. Accessed 2025.
- [4] AccuGlass Products, Inc. UV optical fibers. https://www.accuglassproducts.com/sites/default/files/catalog/fiber_optic_feedthroughs.pdf. Accessed 2025.
- [5] I. H. Malitson. Interspecimen comparison of the refractive index of fused silica. *Journal of the Optical Society of America*, 55(10):1205–1209, 1965.
- [6] Thorlabs, Inc. VUV fused silica plano-convex lenses. https://www.thorlabs.com/newgroupage9.cfm?objectgroup_id=123#. Accessed 2025.
- [7] Edmund Optics, Inc. VUV fused silica plano-convex (PCX) lenses. <https://www.edmundoptics.com/f/uv-fused-silica-plano-convex-pcx-lenses/12410/>. Accessed 2025.
- [8] Andrew S. Glassner, editor. *An Introduction to Ray Tracing*. Academic Press, 1989.
- [9] M. J. D. Powell. An efficient method for finding the minimum of a function of several variables without calculating derivatives. *Computer Journal*, 7(2):155–162, 1964.
- [10] Pauli Virtanen, Ralf Gommers, Travis E. Oliphant, Matt Haberland, Tyler Reddy, David Cournapeau, Evgeni Burovski, Pearu Peterson, Warren Weckesser, Jonathan Bright, Stéfan J. van der Walt, Matthew Brett, Joshua Wilson, K. Jarrod Millman, Nikolay Mayorov, Andrew R. J. Nelson, Eric Jones, Robert Kern, Eric Larson, C. J. Carey, İlhan Polat, Yu Feng, Eric W. Moore, Jake VanderPlas, Denis Laxalde, Josef Perktold, Robert Cimrman, Ian Henriksen, E. A. Quintero, Charles R. Harris, Anne M. Archibald, Antônio H. Ribeiro, Fabian Pedregosa, Paul van Mulbregt, and SciPy 1.0 Contributors. SciPy 1.0: fundamental algorithms for scientific computing in Python. *Nature Methods*, 17:261–272, 2020.
- [11] J. A. Nelder and R. Mead. A simplex method for function minimization. *Computer Journal*, 7(4):308–313, 1965.
- [12] Rainer Storn and Kenneth Price. Differential evolution—a simple and efficient heuristic for global optimization over continuous spaces. *Journal of Global Optimization*, 11(4):341–359, 1997.
- [13] Yang Xiang, Sylvain Gubian, Brian Suomela, and Julia Hoeng. Generalized simulated annealing for global optimization: the GenSA package. *The R Journal*, 5(1):13–28, 2013.
- [14] Y. Xiang and X. G. Gong. Efficiency of generalized simulated annealing. *Physical Review E*, 62:4473, 2000.
- [15] J. Mockus, V. Tiesis, and A. Zilinskas. The application of Bayesian methods for seeking the extremum. In L. C. W. Dixon and G. P.

- Szego, editors, *Towards Global Optimization*, volume 2, pages 117–129. North Holland, 1978.
- [16] Donald R. Jones, Matthias Schonlau, and William J. Welch. Efficient global optimization of expensive black-box functions. *Journal of Global Optimization*, 13(4):455–492, 1998.
- [17] Tim Head, MechCoder, Gilles Louppe, Iaroslav Shcherbatyi, fcharras, Zé Vinícius, cmmalone, Christopher Schröder, nel215, Nuno Campos, Todd Young, Stefano Cereda, Thomas Fan, rene rex, Kejia (KJ) Shi, Jus-
tus Schwabedal, carlosdanielcsantos, Hvass-
Labs, Mikhail Pak, SoManyUsernamesTaken,
Fred Callaway, Loïc Estève, Lilian Besson,
Mehdi Cherti, Karlson Pfannschmidt, Fabian
Linzberger, Christophe Cauet, Anna Gut,
Andreas Mueller, and Alexander Fabisch.
scikit-optimize. <https://scikit-optimize.github.io>. Accessed 2025.
- [18] K. Minschwaner, G. P. Anderson, L. A. Hall, and K. Yoshino. Absorption of solar radia-
tion by O₂: Implications for O₃ and lifetimes
of N₂O, CFCl₃, and CF₂Cl₂. *Journal of
Geophysical Research*, 97(D10):10103–10108,
1992.